# Dynamic permittivity of confined water under a static background field

D. Bratko\* and N. Mulpuri

Department of Chemistry, Virginia Commonwealth University, Richmond, Virginia 23221, United States

**Abstract.** Molecular and collective reorientations in interfacial water are by-and-large decelerated near surfaces subjected to outgoing electric fields (pointing from surface to liquid, i.e. when the surface carries positive charge). In incoming fields at negatively charged surfaces, these rates show a *nonmonotonic* dependence on field strength where fastest reorientations are observed when the field alignment barely offsets the polarizing effects due to interfacial hydrogen bonding. This extremum coincides with a peak of local static permittivity. We use Molecular Dynamics simulations to explore the impact of background static field on high frequency AC permittivity in hydration water under electric field mimicking the conditions inside a capacitor where one of the confinement walls is subject to outgoing and the other one to incoming field. At strong static fields, the absorption peak undergoes a monotonic blue shift upon increasing field strength in both hydration layers. At intermediate fields, however, the hydration region at the wall under incoming field (the negative capacitor plate) features a red shift coinciding with maximal static-permittivity and reorientation-rate. The shift is mostly determined by the variation of the inverse static dielectric constant as proposed for mono-exponentially decaying polarization correlations. Conversely, hydration water at the opposite (positively charged) surface features a monotonic blue shift consistent with conventional saturation. The sensitivity of absorption peaks on the field suggests surface charge densities could be deduced from sub-THz-dielectric spectroscopy experiments in porous materials when interfaces accommodate a major fraction of water contained in the system.

\*dbratko@vcu.edu

# I. INTRODUCTION

Dielectric properties of hydration water are markedly different from those of the bulk liquid<sup>1-17</sup>. Permittivity in the interfacial layer is strongly anisotropic<sup>5, 18-20</sup>. The proximity of apolar confining medium leads to reduced overall permittivity<sup>6, 8, 13, 21</sup>, which is especially prominent in the direction normal to the surface. Spatially resolved profiles of the normal component of the permittivity tensor feature an oscillatory dependence on the distance from the wall(s)<sup>5, 8, 14, 22-26</sup>. The oscillations reflect layered charge-density profiles associated with the distribution of partially charged oxygen and hydrogen atoms in the proximity of the solid. Similar changes affect frequency-dependent permittivity components and the responses to alternating (AC) fields or electromagnetic radiation<sup>6, 27</sup>. In analogy to static permittivity of water in a planar pore, the confinement-induced reduction of both, real and imaginary components of dynamic permittivity is most notable in the normal direction<sup>6</sup>. Lower static permittivities also cause a shift of the absorption peak of the permittivity spectrum to higher frequencies (blue shift). Conversely, lateral components show a more moderate amplitude reduction and a red shift of the spectrum<sup>6</sup>. Both effects are intensified in narrower confinements and play a dominant role in (O(1)nm) micropores. In view of experimental challenges at miniature dimensions, molecular simulation methods<sup>28</sup>, adapted to confined geometries, have played an important role in these studies yet they usually concerned weak fields inside the linear-response regime. Recent analyses<sup>9, 14</sup>, performed at stronger but experimentally relevant fields, revealed strong confinement effects on the nonlinear dielectric response of water. In contrast to conventional dielectric saturation of the bulk aqueous phase, the coupling between aligning field effects and spontaneous polarization of interfacial water was shown to produce a much more complex behavior in the nonlinear regime in confined water. The transition to nonlinear response arises at weaker fields than in the bulk phase and supports nonmonotonic permittivity changes with the field. The effects at opposing confinement walls are asymmetric because of opposite directions of the field relative to the interface. Specifically, simulated dielectric response in water hydrating a planar surface under the incoming field (directed from the liquid to the solid as is the case at a negative electrode) revealed a pronounced permittivity maximum at intermediate field strengths, followed by conventional saturation in stronger fields<sup>14</sup>. An analogous maximum has been observed on isolated surfaces carrying negative charge<sup>29,30</sup>. This nonmonotonic behavior is paralleled by changes in the reorientation dynamics of water molecules. The field strengths corresponding to the peak of local permittivity<sup>14</sup> overlap with the narrow

window of fields reported<sup>31, 32</sup> to give rise to accelerated orientation relaxation in interfacial water. The maxima of local permittivity<sup>14</sup> and collective reorientation rates in the hydration layer next the wall under incoming field<sup>31</sup> are indicative of a balance between the competing effects of fieldalignment and pre-existing orienting preferences next to the surface. On the opposite wall, subjected to the field in outgoing direction, the two orienting trends act in concert and both the static permittivity<sup>14</sup> and molecular reorientation rates<sup>31</sup> decrease monotonically with intensified field. In a capacitor, the two situations correspond to the negatively and positively charged electrode, respectively. The asymmetric change of reorientation dynamics at oppositely polarized walls invites an exploration of water's dielectric response to AC fields in the presence of a static background field, a situation involved e.g. at charged surfaces like membranes or charge-bearing capacitor plates with a superimposed AC signal, e.g. under radiofrequency or microwave radiation. In experiment, the variation of dynamic permittivity in the presence of strong static fields has been thoroughly studied by dielectric spectroscopy in a laterally uniform aqueous film of width  $d_f \sim 260$ nm, subjected to perpendicular static-field strengths of up to 0.01 VÅ<sup>-1</sup> and radiation frequencies between 1-16 GHz<sup>33</sup>. The film was bounded by Si electrodes coated by a thin insulator layer. No signs of dielectric breakdown or DC current have been observed at these conditions. The study revealed a notable saturation; at the strongest field, the real and imaginary components of dynamic permittivity showed up to 70% and 50% reduction, respectively. A blue shift of the absorption peak was also indicated. However, in view of considerable width of the aqueous film, the observed behavior was still dominated by the interior of the film<sup>33</sup>. In the present work, we use Molecular Dynamics (MD) simulations to complement the above experiments with results for a broader frequency range and considerably narrower (~ 2 nm) aqueous confinement, whose overall dielectric response is strongly affected by the contributions from the hydration layers at both walls. The simulated system is pervaded by a static electric displacement field  $D_z=E_o\varepsilon_o$  where  $\varepsilon_o$  is the permittivity of vacuum and  $E_0$  the vacuum field strength at given  $D_z$ . We consider electric displacements of up to ~0.06 C m<sup>-2</sup>, which corresponds to capacitor charge densities of up to an elementary charge per 2.5 nm<sup>2</sup> and averaged strengths of the screened field inside the aqueous film ( $\langle E_{\text{film}} \rangle$ ) of up to 0.049 VÅ<sup>-1</sup>. Comparable charge densities have been considered in studies of nanocapacitors<sup>34</sup> and can be found in biomembranes or functionalized synthetic surfaces<sup>35, 36</sup>, reverse micelles<sup>37</sup> or polyelectrolytes<sup>38-40</sup>. As shown below, the most interesting changes of dielectric properties in hydration layers occur in the interval of  $\langle E_{\rm film} \rangle$  between 0.003 $\sim$ 0.01 VÅ<sup>-1</sup>.

We use MD simulations to estimate responses to a weak oscillatory field of the form  $E_z^{AC}$  =  $E_o^{AC} \sin \omega t$ , where  $\omega = 2\pi v$  is the angular frequency. We consider amplitudes  $E_o^{AC}$  sufficiently small ( $\mu E_0^{AC} \ll kT$ ) to secure a linear response to the AC signal superimposed to the static field  $E_o$ . Here,  $\mu$  is molecular dipole and kT is the thermal energy. The range of  $E_o$  includes intense fields characterized by a strongly nonlinear field-dependence of induced polarization. At these conditions, the dynamic (AC) permittivity does not depend on the comparatively small AC amplitude  $E^o_{AC_{i-1}}$  but is affected by strong background static field. We examine the dependences of both, the real and imaginary components of the differential dielectric constant on the strength of the static field. We determine effective dielectric constants,  $\langle \frac{1}{\varepsilon(z)} \rangle_{ab}^{-1}$ , averaged over aqueous layers between arbitrary lateral planes positioned at  $z_a$  and  $z_b$ , where z is the coordinate normal to the confinement walls. We choose position  $z_a$  and  $z_b$  to envelope the entire water film as well as the regions occupied by the first hydration layer separately for each of the walls, one being affected by incoming and the other by outgoing perpendicular field. In this work, we only consider perpendicular fields and normal (z) components of the permittivity tensor. The subscript z is hence omitted from the notation used in the analysis and the results described in the remainder of the text.

# II. MODEL AND METHODS

Dielectric spectra were extracted from polarization correlation functions in the model system previously considered<sup>14</sup> in a study of dielectric responses to static fields. The system illustrated in Fig. 1 comprises a single pore containing an aqueous film between a pair of parallel, semi-infinite carbon plates mimicking the lattice structure of graphene. The plates are positioned at heights  $z = \pm 9.31$  Å. The interplate (carbon-carbon) separation h is fixed at 18.62 Å, a distance sufficient to accommodate five loosely defined layers of water molecules, thus avoiding appreciable interference between hydration layers at opposite pore surfaces. The laterally extended walls are modeled through periodic replication of the simulation box with volume  $V = L_x L_y L_z = 29.8$  Å x 32.1 Å x 66 Å periodically replicated in x and y directions (parallel to the walls) while there is no periodicity in the normal (z) direction. The height  $L_z$ =66 Å includes 44 Å of empty space, one half below the bottom wall and another half above the top one. In analogy with refs. z=8, 22, 23, 41 and our preceding work z=4, we calculate long range electrostatic interactions under two-

dimensional periodicity using the algorithm of Yeh and Berkowitz, which relies on conventional Ewald summation for a system with increased spacing between pore images in the perpendicular direction, and an explicit, configuration-dependent correction to remove any remaining coupling between the replicas<sup>42</sup>. The plates, containing 364 carbon atoms apiece, were built as described elsewhere<sup>43</sup>. The number of water molecules,  $N_w$ = 458, was determined in an open ensemble (Grand Canonical) Monte Carlo aimulation<sup>44, 45</sup> (GCMC) for identical box in equilibrium with implicit bulk water phase at ambient conditions (excess chemical potential  $\mu_{SPC/E}^{ex} = -11.88 \text{ k} T^{46}$ ) and no electric field. The approach differs from explicit-reservoir calculations<sup>47, 48</sup> where liquid water wets both sides of the walls, allowing dipole attractions across graphene sheets<sup>43, 49</sup>. All simulations under electric field were performed in closed (N, V, T) ensemble MD simulations with fixed number (458) of molecules and without monitoring possible changes in pressure tensor<sup>17,50</sup> due to the field. Atom-atom interactions are described in terms of superimposed coulombic and Lennard Jones potentials of the extended point charge (SPC/E) model for water<sup>51, 52</sup> and we used Lenard-Jones parameters  $\varepsilon_{CC} = 0.277 \text{ kJ mol}^{-1}$  and  $\sigma_{CC} = 3.58 \text{ Å}$  in line with OPLS estimates for sp<sup>2</sup> carbon atoms<sup>53, 54</sup>. GCMC runs used area-integrated water-graphene potential<sup>55</sup> for identical Lennard-Jones parameters. In the first approximation, we neglected the polarizability of graphene<sup>43, 56</sup> and water molecules. The use of SPC/E potential for water establishes a connection with related studies<sup>6-9, 11, 14, 17, 23, 26, 32, 57, 58, 59</sup> of dielectric responses in confined aqueous films. MD

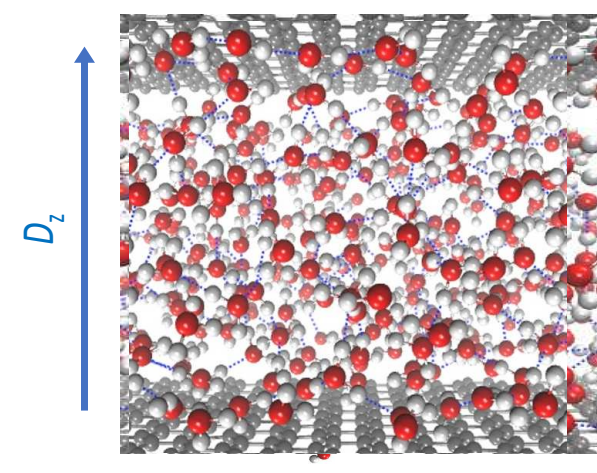


**Fig. 1** Side view of an MD configuration of water in the elementary box: Gray atoms belong to parallel graphene walls of approximate size  $L_x L_y \cong (3 \text{ nm})^2$  separated by distance  $h \cong 1.86 \text{ nm}$ . The system is periodically replicated in lateral (xy) directions.

simulations were performed using the Gromacs package<sup>60</sup> at (*N*, *V*, *T*) conditions, with *T* held at 300 K. As already discussed, Coulombic interactions include pseudo-two-dimensional particle mesh Ewald (PME) summation<sup>61</sup> with slab-correction<sup>42</sup> and increased inter-replica separation in *z* direction. Thermostatting relied on velocity rescaling<sup>62</sup> with a stochastic term and a 100 fs time constant. Equations of motion were propagated using the Leap-Frog algorithm with timestep of 1 fs and samples were taken every 2fs. Molecular rigidity was enforced by the LINCS algorithm<sup>63</sup>, <sup>64</sup>. At each field strength, the system was equilibrated for at least 11 ns followed by 16 ns production runs. Empirically, long equilibration times were found to improve the reproducibility of calculated time correlation functions for polarization fluctuations.

Calculations correspond to a sequence of simulated inter-plate voltages  $U = \psi_{top} - \psi_{bottom} = -\int_{z_{bottom}}^{z_{top}} \langle E(z) \rangle dz$  resulting from imposed electric displacements  $D_z$  listed in Table 1.  $z_{top}$  and  $z_{bottom}$  are the positions of the top and bottom pore walls positioned parallel to xy plane and  $\langle E(z) \rangle$  is the canonical average of the perpendicular (z) component of dielectrically screened field vector at distance z from the pore midplane at z=0. As only the perpendicular component of the field has a nonvanishing average, we omit subscript z in all equations describing the systems's electrostatics. We determine  $\langle E(z) \rangle$  according to the relation  $\langle E(z) \rangle = \frac{D_z - \langle m(z) \rangle}{\varepsilon_o}$ , where m(z) is the local polarization density associated with charge density  $\rho_q(z) = \frac{1}{L_x L_y} \sum_i q_i \, \delta(z_i - z)$  arising from partial charges  $q_i$  of oxygen and hydrogen atoms at positions  $z_1^{23,65}$  in the course of the simulation:

$$m(z) = -\int_{-\infty}^{z} \rho_a(z')dz' \tag{1}$$

Calculations of simulated atom and charge density and resulting polarization profiles in the pore at given voltages have been described in the preceding work<sup>14</sup>. Because of the spontaneous polarization related to the interfacial structure of water, simulated profiles m(z) feature strong oscillations even in the absence of external field (vanishing voltage U). The results for a sequence of electric displacements  $D_z$  listed in Table I showed<sup>14</sup> the profiles m(z) to become increasingly asymmetric and the screened field <E> and voltage U deviate from a linear dependence on the applied electric displacement<sup>14</sup>. In addition to calculated voltages U and position-independent vacuum fields  $E_0$ = $D_z \varepsilon_0^{-1}$ . Table I lists screened fields <E> and <E $_1$ P averaged across the entire pore or over the narrower region corresponding to aqueous film with nonzero simulated charge

density  $\langle \rho_q(z) \rangle$ , respectively. The averages pertaining to the aqueous film (defined above) are significant as they exclude the contributions of vacant regions within the wall-atom contact distances<sup>66</sup> that do not affect water molecules. The calculations of simulated atom, charge and polarization profiles in the pore for given voltages have been described in the preceding work<sup>14</sup>. With the above force fields, simulated charge densities generally vanish at  $\sim 1.09$  Å from carbon walls<sup>6, 14</sup>, leading to the estimated film thickness of 16.44 Å for wall-wall separation of 18.62 Å used in our study.

Integration of m(z) over an arbitrary region  $z_a \le z \le z_b$  yields the dipole moment  $M_{ab}$  between the lateral planes at  $z_a$  and  $z_b$ 

$$M_{ab} = L_x L_y \int_{z_a}^{z_b} m(z') dz'$$
 (2)

**Table 1.** Imposed electric displacements  $D_z$ , corresponding to vacuum fields  $E_0 = D_z \varepsilon_0^{-1}$ , voltages U defined as the difference between simulated electrostatic potentials at opposing graphene sheets  $U = \psi_{top} - \psi_{bottom}$ , average electric field between graphene sheets,  $\langle E \rangle$ , and inside the aqueous film,  $\langle E_f \rangle$ . The film corresponds to the region characterized by finite charge density  $\rho_q$  originating from partial charges on atoms of water molecules.

$D_z/\mu\mathrm{C~cm}^{-2}$	E <sub>o</sub> / VÅ <sup>-1</sup>	U/V	<e> / VÅ<sup>-1</sup></e>	$\langle E_{\rm f} \rangle / \mathrm{VÅ^{-1}}$
0	0	0	0	0
0.22	0.025	-0.0705	0.0038	0.00097
0.44	0.05	-0.140	0.0075	0.00193
0.71	0.08	-0.225	0.0121	0.00308
0.97	0.11	-0.310	0.0166	0.00433
1.33	0.15	-0.428	0.023	0.00618
1.77	0.20	-0.577	0.031	0.00867
2.66	0.30	-0.889	0.0477	0.0144
4.43	0.50	-1.578	0.0847	0.0299
6.20	0.70	-2.326	0.140	0.0487

where we omit vectorial notation since averaged  $M_{ab}$ =(0,0, $M_{ab}$ ) has vanishing lateral components.

As detailed below, we apply Eq. (2) with  $z_a$  and  $z_b$  representing the boundaries of hydration layers located between the distances of 1.09Å and 4Å from either graphene plate where the latter value corresponds to the first minimum of the wall/water atom density distribution<sup>14</sup>. Similarly, we obtain the total dipole moment in the simulation box, M, according to

$$M = L_x L_y \int_{-\infty}^{\infty} m(z') dz' \equiv L_x L_y \int_{z_{bottom}}^{z_{top}} m(z') dz'$$
 (3)

Correlations between the regional polarizations,  $M_{ab}$ , and the total polarization, M, provide the effective value of the inverse differential dielectric constant in a specified volume<sup>5,14</sup>, between  $z_a$  and  $z_b$ ,  $V_{ab} = L_x L_y (z_b - z_a)$ 

$$\frac{1}{\varepsilon_{eff}} = <\frac{1}{\varepsilon(z)}>_{ab} = 1 - \frac{\beta}{V_{ab}\varepsilon_{o}} \left[ < M_{ab}M > - < M_{ab} > < M > \right]$$
 (4)

where  $\beta = \frac{1}{kT}$ . As noted in ref.<sup>41</sup>, Eq. (4), appropriate for a single pore with no periodicity in the normal direction<sup>5-8, 14, 17, 22, 23, 41</sup>, differs from the related expression<sup>18</sup> for physically distinct systems periodic in all three dimensions<sup>18, 19, 26, 67</sup>. The reader is referred to ref.<sup>8</sup> and associated Supporting Information for elaborate discussion of the two scenarios. Static dielectric constants  $\varepsilon_{eff}$  along the perpendicular direction, determined by applying Eq. (4) separately to each hydration layer and the entire water film for a range of electric displacements, have been reported in the preceding work<sup>14</sup>. At higher voltages (Table I), simulations revealed a strongly nonlinear dielectric response with remarkable differences between hydration layers at the walls with opposite (incoming  $\nu$ s outgoing) directions of the field relative to the nearer wall<sup>14</sup>.

Generalization to alternating fields involves the imaginary, frequency-dependent permittivity  $\varepsilon(\nu) = \varepsilon'(\nu) - i\varepsilon''(\nu)$ . In the limit of zero-frequency ( $\nu = 0$ ), Eq. (4) provides the real part  $\varepsilon'(0)$  while  $\varepsilon''(0) \to 0$ . At finite frequencies  $\nu$ , we obtain effective values of  $\varepsilon'(\nu)$  and  $\varepsilon''(\nu)$  in a specified region  $V_{ab}$  from the temporal polarization-correlation function<sup>6</sup>:

$$\Phi_{ab}(t) = \langle M_{ab}(0)M(t) \rangle - \langle M_{ab} \rangle \langle M \rangle \tag{5}$$

As in preceding equations, we consider only perpendicular components of vectorial quantities M, hence we omit the subscript z in our notation. The perpendicular (z) component of the permittivity tensor  $\varepsilon(\nu)$  in the region between  $z_a$  and  $z_b$  can then be expressed as<sup>6</sup>

$$\frac{1}{\varepsilon_{ab}(\nu)} = \langle \frac{1}{\varepsilon(z;\nu)} \rangle_{ab} = 1 - \frac{\beta L_s(-\Phi'_{ab}(t))}{\varepsilon_o V_{ab}} \equiv 1 - \frac{\beta [\Phi_{ab}(0) - sL_s(\Phi_{ab}(t))]}{\varepsilon_o V_{ab}}$$
(6)

where  $s=i2\pi\nu$ ,  $\Phi'_{ab}(t)$  is the time derivative of  $\Phi_{ab}(t)$  and  $L_s(f(t))=\int_0^\infty e^{-st}f(t)dt$  is the Laplace transform of function f(t). Eq. (6) reduces to Eq. (4) at vanishing  $\nu$  and s.

In the present work we use Eq. (6) to characterize the response to an oscillatory field of the form  $E_z^{AC} = E_0^{AC} \sin 2\pi \nu t$  with frequencies  $\nu$  from 0 to  $10^{15}$  Hz, when the AC field is superimposed to static field E(z). In experiment, the above situation can be observed in a charged microcapacitor or in the vicinity of an electrified surface with the AC component of the field introduced by linearly polarized electromagnetic radiation propagating in lateral direction. In the simulation, we characterize the frequency-dependent permittivity from polarization fluctuations according to the fluctuation-dissipation relation, which does not require an explicit introduction of the AC signal into the simulated system. While we limit our analysis to weak alternating fields  $(\frac{\mu E_0^{AC}}{kT} \ll 1)$ , it is important to note we consider strong background DC fields with  $\mu E_0^{DC}$  comparable to kT, which affect the magnitude of polarization fluctuations and temporal polarization correlation functions  $\Phi_{ab}(t)$ , Eq. (5). As such, the static electric displacement effectively modulates the AC permittivity in the system. Known asymmetric effects of static fields on structural and dynamic properties of hydration layers under incoming and outgoing fields require separate characterizations of AC permittivities within hydration layers at opposing walls of the pore. For short times t, the accuracy of computed  $\Phi_{ab}(t)$  was shown to depend on the bin size used to determine charge density and polarization profiles. The size effect can be checked by comparing static dielectric constants  $\varepsilon'(\nu)$  determined from polarization change due to a finite field with those obtained from polarization correlation function value at t=0,  $\Phi_{ab}(0)$ . Correlation functions  $\Phi_{ab}(t)$  were hence computed from polarization profiles obtained using 880 and 1760 bins followed by extrapolation of  $\Phi_{ab}(t)$  to vanishing bin size, which produced an excellent agreement

between alternative routes to  $\varepsilon'(\nu)$ . Since our force fields neglect internal degrees of freedom of water molecules and polarization effects of carbon atoms, predicted dielectric constants include only configurational contributions for *rigid* molecules, which represents a reasonable approximation within the sub-THz regime characterized by the Debye behavior<sup>68</sup>.

# III. Results and discussion

In this section, we report simulated responses to AC signals in the presence of a strong static (DC) field encountered e.g. inside a capacitor or in the vicinity of an electrified interface. Covering a broad range of static fields, we consider a set of systems with electric displacements  $D_{\rm z}$  and associate wall-to-wall voltages U (Table I), previously characterized in the absence of the AC component<sup>14</sup>. Charge density, polarization and static permittivity profiles for different values of  $D_z$  have been described elsewhere <sup>14</sup>. Based on verified continuity of distributions <sup>69</sup> for the above structural quantities, there has been no indication of electrofreezing<sup>70-73</sup> in given voltage range and ambient temperature, although it would likely be indicated if lowered temperatures were also considered. All of the above quantities inside a planar pore show considerable asymmetry, associated with different orientational polarizabilities of interfacial water at the two surfaces, one subjected to incoming and another to outgoing static field. Specifically, the static permittivity inside the hydration layer under the incoming field can be more than twice higher than its counterpart at the opposite wall. Because of the direct relation between static dielectric constant and the frequency-dependent permittivity at finite  $\nu$ , analogous asymmetry is observed with real and imaginary parts of  $\varepsilon(\nu) = \varepsilon'(\nu) - i\varepsilon''(\nu)$ . As shown by Gekle and Netz<sup>6</sup>, when the polarization time correlation function  $\Phi_{ab}(t)$  features an approximately exponential decay, the peak frequency  $v_{max}$  of the imaginary component  $\varepsilon''(v)$  (inflection frequency of the real component  $\varepsilon'$ ) can be estimated from

$$\nu_{max} \cong \frac{1}{2\pi\tau_{\Phi}\varepsilon'(0)} \tag{7}$$

where  $\tau_{\Phi}$  is the correlation time of  $\Phi(t)$ 

$$\tau_{\Phi} = \frac{\int_0^{\infty} \Phi(t) dt}{\Phi(0)} \tag{8}$$

Calculations of  $\varepsilon(v) = \varepsilon'(v) - i\varepsilon''(v)$  (Eq. 6) and  $\tau_{\Phi}$  (Eq. 8) require accurate simulation data for  $\Phi_{ab}(t)$  within pore regions ab over long time-intervals characterized by non-negligible magnitudes  $\Phi_{ab}(t)$  as needed for accurate Laplace transform calculations. Precision of  $\Phi_{ab}(0)$  is of utmost importance. As noted above, accurate  $\Phi_{ab}(t)$  relied on the use of tiny bins for m(z) calculation and subsequent extrapolation to vanishing bin size and we used fitted functions  $\Phi_{ab}(t)$  in analytic Laplace transformations.

A. Polarization correlation function. Fig. 2 illustrates the form of  $\Phi_{ab}(t)$  associated with perpendicular (z) polarization for the entire pore in the absence of external field. In this and all other examples concerned with individual hydration layers, either with or without applied field, the long-time behavior was well described by exponential relaxation whereas the short-time regime affected by H-bond libration dynamics followed a damped oscillatory behavior of the form  $\cos(\frac{2\pi t}{\tau_l})e^{-At}$  with the libration period  $\tau_l$  of 36±1 fs. Both functional forms allow analytic Laplace transformation. Specifically,

$$L_s[e^{-At}] = \frac{1}{s+A}$$
 and  $L_s[\cos(\frac{2\pi t}{\tau_l})e^{-At}] = \frac{s+A}{(s+A)^2 + (\frac{2\pi}{\tau_l})^2}$  (9)

where  $s=i2\pi\nu$ . In all pore regions and at arbitrary conditions, robust fitting of  $\Phi_{ab}(t)$  was possible by approximating  $\Phi_{ab}(t)$  with a linear combination of at least four distinctly parameterized terms, two of exponential and two of damped-oscillatory form. Several formulae satisfying the above requirement were found to produce essentially identical  $\varepsilon(\nu)$ . All spectra  $\varepsilon(\nu)$  reported below are based on a 7-parameter fitting function of the following form:

$$\Phi_{ab}(t) \cong \tag{10}$$

$$\Phi_{ab}(0) \left[ A_0 \cos \left( \frac{2\pi t}{\tau_l} \right) \left[ A_1 \, e^{-A_2 t} + (1-A_1) e^{-A_3 t} \right] + (1-A_0) \left[ A_4 \, e^{-A_5 t} + (1-A_4) e^{-A_6 t} \right] \right]$$

with parameters  $A_1$  (i=0-6) for each individual case determined by the xmgrace nonlinear-curve fitting<sup>74</sup> of simulation results.  $A_0$ ,  $A_1$  and  $A_4$  are dimensionless constants with typical values between  $0.6\pm0.1$ ,  $0.4\pm0.1$ , and  $0.4\pm0.2$ , respectively. Time decay constants  $A_2$ ,  $A_3$ ,  $A_5$  and  $A_6$  correspond to reciprocal relaxation times for exponential terms. Typical values of  $A_2^{-1}$  and  $A_5^{-1}$ 

were of  $O(10^{-1})$  ps and  $A_3^{-1}$  and  $A_6^{-1}$  were of  $O(10^{-2})$  ps. Depending on the quality of simulated  $\Phi_{ab}(t)$  at longer times, the fitting procedure relied on simulation inputs over times t of 3-6 ns. Fig. 2 includes a comparison between the simulated (black) and fitted (blue) curves in the absence of static field. Qualitative features and the oscillation period are common to all domains in the confinement and show complete agreement with previous works  $^{6,75}$ . In view of Eq. (4), the initial values  $\Phi_{ab}(0)$  for specified volume  $V_{ab}$  are proportional to  $(1-\frac{1}{\varepsilon_{eff}})$  for given volume. For the present system, average static dielectric constants in hydration layers and electric displacements listed in Table I were found  $^{14}$  to span the range between  $\sim 5$  to 57, which translates to up to 25% variation of  $\Phi_{ab}(0)$ . The fitting of  $\Phi_{ab}(t)$  in hydration layers was of comparable quality as for the entire pore and the convergence was not affected by the magnitude of the static electric displacement.

**B.** Correlation time. Simulations performed with the same model of water in the linear response regime revealed<sup>51</sup> remarkably stable correlation times  $\tau_{\Phi}$  of around 145±50 fs, a result essentially independent of confinement effects<sup>6</sup>. Our and others'earlier MD studies in the nonlinear regime revealed significant, polarity-dependent changes of molecular reorientation dynamics in hydration layers<sup>31, 32, 76, 77</sup>. However, our present results confirm these changes are not reflected in comparable effects on decay rates of correlation functions  $\Phi_{ab}(t)$ , which depend on the dynamics

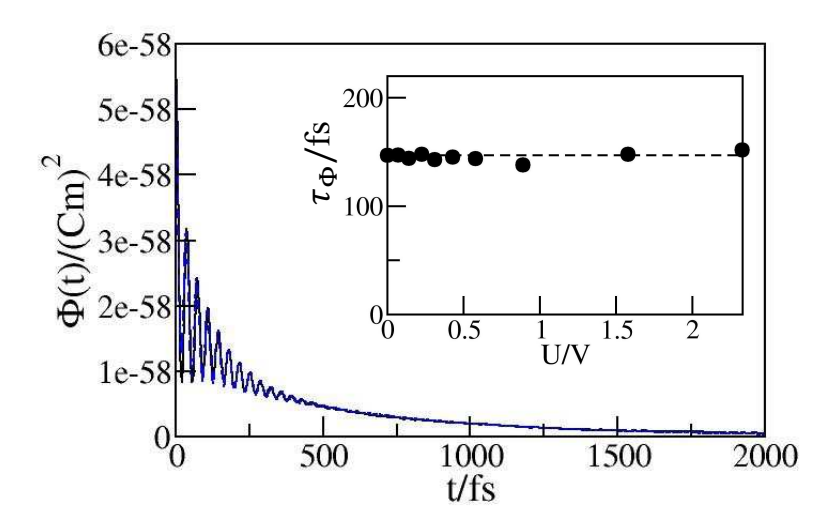
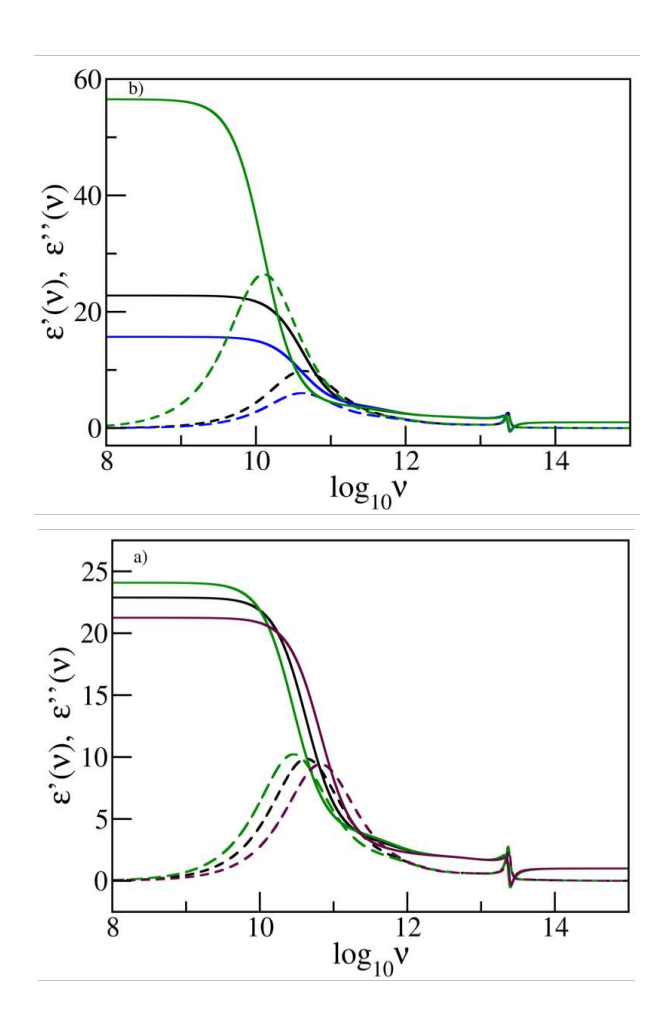


Fig. 2 Simulated correlation function  $\Phi(t)$ , Eq. (5) (black) and fitted function from Eq. (10) (blue) for the entire box in the absence of static field (U=0). Inset: correlation times  $\tau_{\Phi}$ , Eq. (8), observed at different wall-to-wall voltages U do not reveal statistically significant field effects on the rate of correlation decay.

of global polarization<sup>6</sup>, in addition to that of individual hydration layers. In the inset of Fig. 2 we include new results for correlation times  $\tau_{\Phi}$  at varied voltages including voltage values well outside the linear response regime of DC polarization. The correlation time associated with the total polarization M shows only minor effects of voltage U. When considering correlation times of functions  $\Phi_{ab}(t) = \langle M_{ab}(0)M(t) \rangle - \langle M_{ab} \rangle \langle M \rangle$  with subscripts ab denoting the volume of either hydration layer, occasional molecular recrossings between the layer and the aqueous core introduce some ambiguity to calculated correlation times,  $\tau_{\Phi}$ . Nonetheless, the  $\tau_{\Phi}$  values based on  $\Phi_{ab}(t)$  and  $M_{ab}$  of individual hydration layers were generally found to persist within the context-independent window of 145±50 fs originally established<sup>6</sup> within the linear response regime.

C. Dynamic permittivity. In Figs. 3 and 4, we examine the effect of static electric displacement on the frequency-dependent permittivity  $\varepsilon(\nu) = \varepsilon'(\nu) - i\varepsilon''(\nu)$  in the slit. Given the choice of our model of water<sup>51</sup>, these results reflect the contributions from the orientational polarization, which are dominant below THz frequences. Notwithstanding the omission of high frequency terms arising from internal degrees of freedom in real water<sup>68</sup>, in Fig. 3 we include the results from given model for  $\varepsilon(v)$  at frequences of up to PHz to illustrate the apparent librational peak of  $\varepsilon''(\nu)$  predicted by the SPC/E model around 25 THz. Consistent with the independence of the oscillation frequency  $\Phi_{ab}(t)$  from voltage U, the librational peak is essentially identical at all external fields. The results presented in Figs. 3 and 4 also exclude the optical term of  $\sim 1.75$  that should be added when making comparisons with experiments. In Fig. 3 we compare dielectric spectra in the absence of static field ( $D_z$ =0) with those corresponding to a moderate electric displacement  $D_z$ =0.71  $\mu$ C cm<sup>-2</sup> (U = - 0.225 V), at which we observe the maximum of static permittivity  $\varepsilon'(0; U)^{-14}$  and the fastest reorientation dynamics in hydration water under an incoming (pointing from liquid to solid) field<sup>31</sup>. Fig.3a illustrates frequency dependences of real and imaginary parts,  $\varepsilon'(\nu)$  and  $\varepsilon''(\nu)$  at zero DC field averaged over the entire slab (black), the aqueous core (excluding hydration water, brown), and hydration layers (green). Because  $D_z=0$ , both hydration layers have identical dielectric responses. The general features of the spectra for frequencies  $\nu$  of up to 0.1 THz resemble those uncovered in the work by Gekle and Netz<sup>6</sup> and Andrade et al.21 in showing a considerable shift of the absorption maximum of the entire system to higher frequency (blue shift) compared to bulk water. Somewhat unexpectedly, our results are also indicative of a shift in the central aqueous core because our slit is too narrow to accommodate

a core interior resembling bulk water. The relative shifts are consistent with the comparatively higher static permittivity<sup>14</sup> within hydration layers, leading to lower values of  $\nu_{max}$  predicted by Eq. (7).



**Fig. 3** a) Frequency dependencies of the real (solid lines) and imaginary (dashed lines) parts of dielectric constant in the hydration layers (green), in the film interior (brown), and over the entire film (black) in the absence of applied field. (b) Real (solid lines) and imaginary (dashed lines) parts of permittivity in the bottom hydration layer (blue), the entire aqueous film (black) and the top wall hydration layer (green) at applied voltage U=-0.225 V. In the absence of applied voltage (a), red shift (to lower frequencies) is seen in both hydration layers (green), while we observe a blue shift in the core region (brown). Applied voltage U=-0.225 V (b) leads to a notable increase in the static dielectric constant along with concomitant red shift in the top hydration layer with incoming field (green). Conversely, static dielectric constant in the bottom hydration layer (outgoing field) decreases and a moderate blue shift is observed (blue) due to the static field. While our model does not capture high-frequency features associated with intramolecular events<sup>55</sup>, we include model results above 1 THz to illustrate the libration-related peak introduced through oscillations of  $\Phi(t)$ , Fig. 2.

Fig. 3b shows analogous results in the presence of wall-wall DC voltage U=-0.225 V. Here, the static permittivity  $\varepsilon'(0)$  in the hydration layer under incoming field (the initial plateau

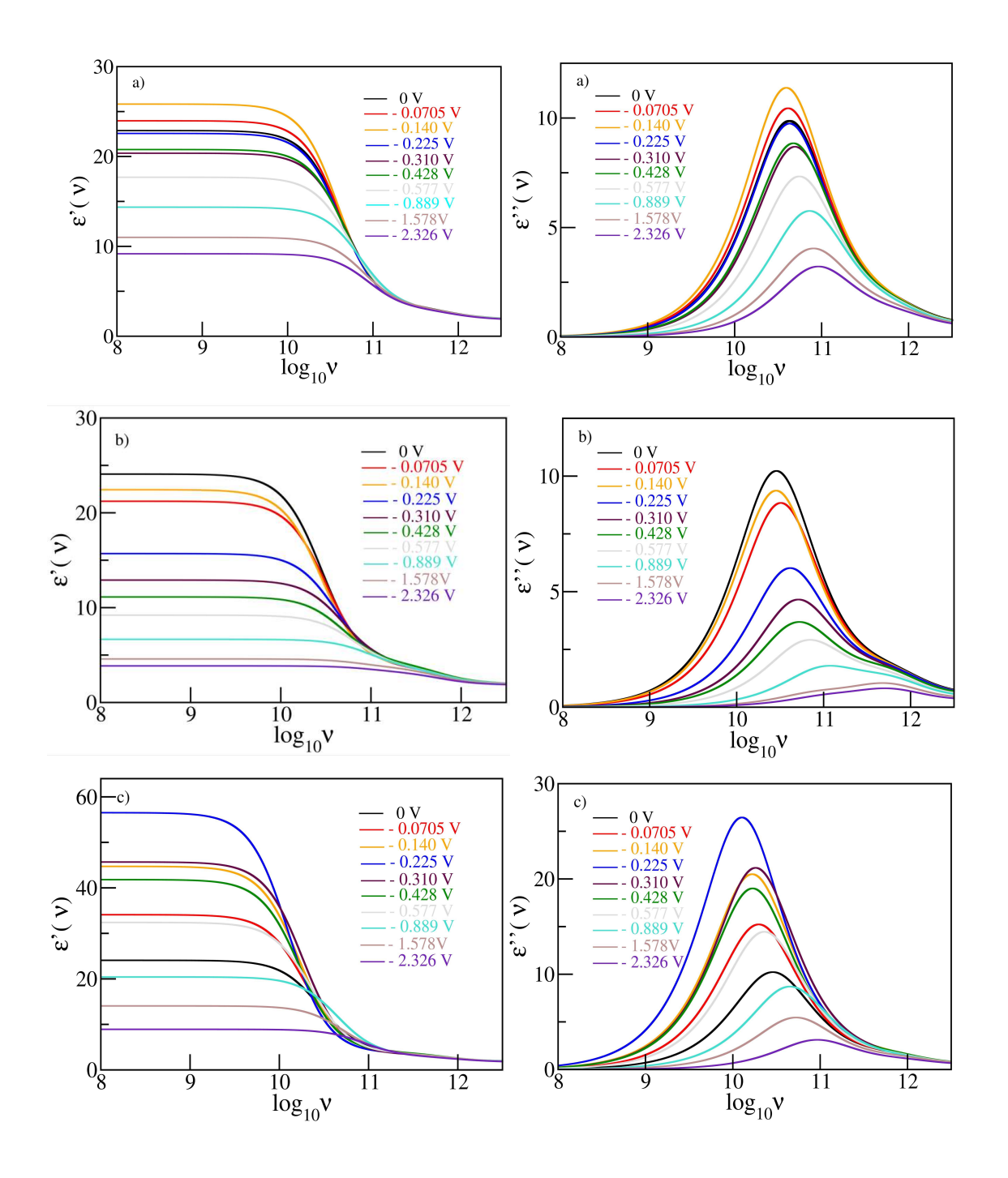


**Fig. 4** Frequency dependencies of real (left) and imaginary parts (right) of permittivity averaged over the entire aqueous film (a), the bottom hydration layer (b), and the top hydration layer (c) at different voltages between the positions of the two graphene sheets  $U = \psi_{top} - \psi_{bottom}$ .

value of the solid green curve) greatly exceeds the value corresponding to the field with outgoing direction (plateau of the solid blue curve). In accordance with Eq. (7), this difference contributes to a red spectral shift in the former and blue shift in the latter scenario (dashed green and blue curves in Fig. 3b, respectively).

The nonmonotonic variation<sup>14</sup> of the perpendicular component of static permittivity  $\varepsilon'(0)$  suggests a similar pattern to apply to the spectral shift (repositioning of  $v_{max}$ ) as a function of the wall-to-wall voltage U. This prediction is borne out by the spectra collected in Fig. 4 for all voltages considered in Table 1. Most remarkably, the absorption peak in the hydration layer under incoming field shows a red shift reflecting the increase in  $\varepsilon'(U; v = 0)$  with U until reaching the voltage around U=-0.225 V, which maximizes  $\varepsilon'(0)$ . Further increase in U leads to gradual increase in  $v_{max}$ . The spectral shift in the hydration layer under outgoing field, on the other hand, is monotonic in agreement with the monotonic reduction of respective  $\varepsilon'(U; v = 0)^{14}$ . These trends are summarized in Fig. 5, which shows the dependence of  $v_{max}$  on the applied voltage U for the entire aqueous film (black) and hydration layers under incoming (green) or outgoing (blue) field.

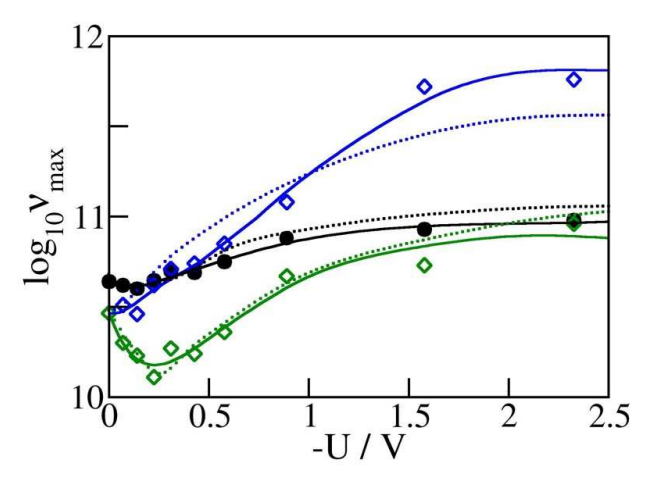


Fig. 5 Frequences corresponding to the maxima of the imaginary component of the dielectric constant in the bottom hydration layer (blue), in the entire aqueous film (black), and the top hydration layer (green) as functions of the wall-wall voltage U. Solid curves show a smooth fit through simulation results (symbols). Dotted curves follow the prediction  $v_{max} \cong (2\pi\tau_{\Phi}\varepsilon_{\perp})^{-1}$  based on presumed mono-exponential decay of time correlation functions. The monotonic blue shift in the bottom hydration layer (blue), and nonmonotonic behavior in the top hydration layer (incoming field, green) are primarily affected by changes of  $\varepsilon_{\perp}$ , whose maximum gives rise to the minimum of  $v_{max}$  in the top hydration layer (green), with any changes of the correlation time  $\tau_{\Phi}$  playing a minor role.

At the surface under incoming field (negative charge), a rapid nonmonotonic variation of  $v_{max}$  takes place over a narrow window of voltages U.

In Fig. 5, we also include a comparison between the simulation results for the absorption peak frequencies taken from the spectra in Fig. 4 and the predictions of Eq. (7),  $v_{max} \cong \frac{1}{2\pi\tau_{\Phi}\varepsilon'(0)}$  (dotted curves). These curves were obtained by using smooth functions  $\tau_{\Phi}(U)$  and  $\varepsilon'(0; U)$  fitted through simulation data for the entire set of voltages. We include results calculated separately for individual hydration layers and for the entire water slab. The comparison confirms a qualitative validity of Eq. (7) but shows quantitative differences, which we attribute to the deviations of actual correlation functions  $\Phi_{ab}(t)$  (see Fig. 2) from the mono-exponential functional form presumed in the derivation of Eq. (7). In view of relatively stable value of  $\tau_{\Phi}(U)$  irrespective of the voltage and specific region in the confinement, the changes of  $v_{max}$  are primarily associated with varying  $\varepsilon'(0; U)$ . According to Fig. 5, absorption spectra can be effectively tuned by varying the strength of static electric field or, equivalently, the surface charge density of the confining walls. Alternatively, the relation between the absorption peak frequency and the strength of the field can be used to inform us about the surface charge in the system.

According to Fig. 4, the effect of static field is not limited to shifting the spectrum of permittivity components but also causes large variations in the absolute values of  $\varepsilon'(\nu)$  and  $\varepsilon''(\nu)$ . The amplitudes of both components by-and-large reflect the reported variation of the average static dielectric constants  $\varepsilon'(U; \nu = 0)$  of the entire aqueous slab or for separate hydration layers. This relation leads to a strongly nonmonotonic dependence of both the real and imaginary permittivity components on the applied voltage in the hydration layer under the incoming field. Fig. 6 illustrates the voltage dependences of maximal real and imaginary components,  $\varepsilon'(U; \nu = 0)$  (solid symbols) and  $\varepsilon''(U; \nu = \nu_{max})$  (open symbols) averaged over the entire aqueous film (black) or hydration layers under incoming (green) and outgoing (blue) field. The nonmonotonic variation of the static permittivity is clearly reflected in the variation of the imaginary component, whose peak magnitude is typically close to  $\frac{1}{2}$  of  $\varepsilon'(U; \nu = 0)$ . As with the static permittivity, the nonmonotonic variation of the imaginary permittivity with the voltage is limited to the hydration region subject to incoming static field while the remaining regions feature a monotonic decrease with U akin to conventional saturation. While our present calculations

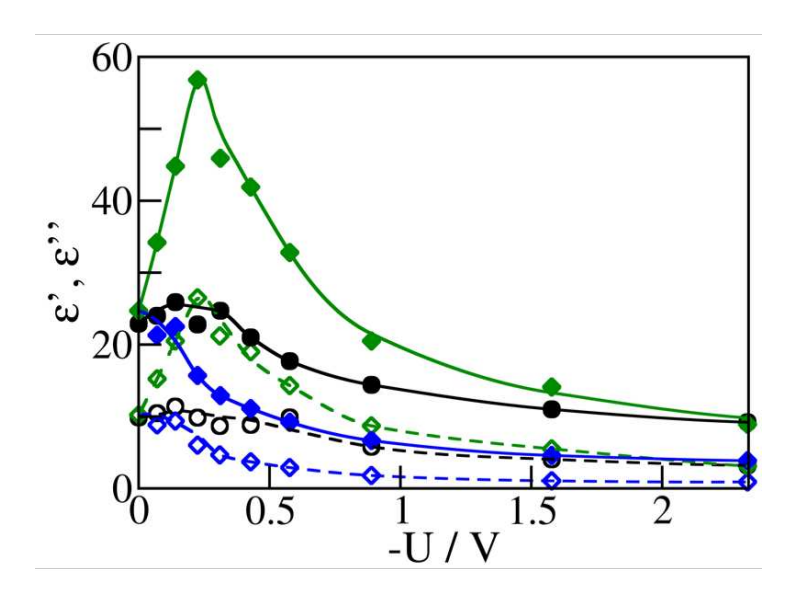


Fig. 6 Spatially averaged static dielectric constants  $\varepsilon'(0)$  (real components of relative permittivity at zero frequency, solid symbols), and the peak values of the imaginary components  $\varepsilon''(\nu_{max})$  (open symbols) of the frequency-dependent dielectric constants. Black, blue, and green color denote the averages over the entire water film and hydration layers at the bottom and the top wall, respectively. The horizontal (x) axis shows the inter-wall voltage  $U = \psi_{bottom} - \psi_{top}$ . Effective values of dielectric constant components are based on averaged reciprocal values, i.e.  $\varepsilon^{\alpha}(U) = \langle \frac{1}{\varepsilon^{\alpha}(z;U)} \rangle_{z}^{-1}$ .

concern hydration water in a narrow confinement, a similar qualitative behavior can be generalized to hydration water layers next to isolated electrified surfaces like ionized membranes or liquid crystal interfaces. In these cases, the nontrivial dependence of permittivity on the extent of ionization is expected at negatively charged surfaces whereas the variation next to positive ones should resemble a usual saturation regime. By the same token, asymmetric dielectric screening of both DC and AC fields should be expected in the vicinity of a dipolar colloidal particle<sup>78</sup> with antisymmetric surface charge distribution. Salt screening<sup>79, 80</sup> can potentially weaken but not overturn this behavior.

# IV. CONCLUDING REMARKS

Outside the linear response regime, the permittivity of hydration water has been shown to depend on the direction of electric field relative to the interface<sup>14</sup>. As a result, a perpendicular DC field applied across a confinement can give rise to markedly different *static* dielectric constants in the proximities of the two confining walls. In the present study, we examine concomitant effects

of static field on dielectric responses to high-frequency AC signals, a situation encountered e.g. in a dielectric spectroscopy measurement inside a charged micro-capacitor, or in a dispersion with a significant fraction of hydration water next to isolated electrified surfaces. The nonlinear regime sets in at unscreened fields as low as 10<sup>-2</sup> V Å<sup>-1</sup> <sup>14</sup>, corresponding to realistic surface charge densities of an elementary charge per O(10<sup>2</sup>) nm<sup>2</sup>. Preceding studies revealed a strong dependence of molecular reorientation rates of water molecules on the polarity of the electric field pervading the hydration layer. Deceleration has been observed near surfaces subjected to an outgoing static field (pointing from surface to liquid) as is the case when the solid carries positive charge. In an *incoming* field (next to negatively charged surfaces), both the reorientation rates and local permittivity in the hydration layer showed nonmonotonic dependences on the field strength with the fastest reorientations<sup>31</sup> and highest permittivity<sup>14</sup> observed when the field alignment barely offsets the orienting bias at the wall. Using Molecular Dynamics simulations, we explore the impact of background field (or, equivalently, surface charge density) on high frequency (GHz to THz) AC permittivity in hydration water inside a nanosized aqueous film under perpendicular DC fields commensurate with surface charge densities from 0 to  $\sim 0.4$  elementary charges per nm<sup>2</sup>. Our model system mimics conditions inside a capacitor where one of the confinement walls is subject to outgoing and the other one to incoming field. In very strong static fields, the frequency corresponding to the maximal imaginary part of AC permittivity features a blue shift with increasing field strength in both hydration layers. At intermediate fields, however, the hydration region at the wall under ingoing field (adjacent to the negative capacitor plate) features a red shift, which is especially pronounced at the field strength corresponding to the maxima of staticpermittivity and reorientation-rate. The spectral shift inside the hydration layer reflects the variation of the inverse static dielectric constant and associated polarization amplitude<sup>6</sup> but does not appear affected by the changes in local reorientation rates of water molecules. Hydration water at the opposite surface (the positive capacitor plate), on the other hand, features a monotonic blue shift consistent with conventional saturation. The sensitivity of imaginary peaks on the field suggests surface charge densities could be deduced from sub-THz dielectric spectroscopy experiments in a porous material where hydration layers comprise a major fraction of water contained in the system.

#### **ACKNOWLEDGMENTS**

We acknowledge National Science Foundation for support (award CHE-1800120), and National Energy Research Scientific Computing Center (NERSC), funded by the Office of Science of the U.S. Department of Energy (No. DEAC02-05CH11231) and Extreme Science and Engineering Discovery Environment (XSEDE), funded by NSF Grant No. OCI-1053575 for supercomputing time allocations.

#### **AUTHOR DECLARATIONS**

#### **Conflicts of interest**

The authors have no conflicts to disclose.

#### **Author Contributions**

**D. Bratko**: Conceptualization (leading); Investigation (equal); Formal analysis (equal); Validation (equal); Writing, (leading), Data curation (equal). **N. Mulpuri**: Computations (leading); Investigation (equal); Formal analysis (equal); Validation (equal); Writing (supporting); Data curation (equal).

#### **DATA AVAILABILITY**

The data that support the findings of this study are available from the corresponding author upon reasonable request.

#### References

- <sup>(1)</sup> K. Morikawa, Y. Kazoe, K. Mawatari, T. Tsukahara, and T. Kitamori, *Anal. Chem.* **87**, 1475 (2015).
- B. Natarajan, C. Emiroglu, J. Obrzut, D. M. Fox, B. Pazmino, J. F. Douglas, and J. W. Gilman, *ACS Appl. Mater. Interfaces* **9**, 14222 (2017).
- <sup>(3)</sup> L. Fumagalli, A. Esfandiar, R. Fabregas, S. Hu, P. Ares, A. Janardanan, Q. Yang, B. Radha, T. Taniguchi, K. Watanabe, G. Gomila, K. S. Novoselov, and A. K. Geim, *Science* **360**, 1339 (2018).
- <sup>(4)</sup> A. Montenegro, C. Dutta, M. Mammetkuliev, H. T. Shi, B. Y. Hou, D. Bhattacharyya, B. F. Zhao, S. B. Cronin, and A. V. Benderskii, *Nature* **594**, 62 (2021).
- (5) D. J. Bonthuis, S. Gekle, and R. R. Netz, *Phys. Rev. Lett.* **107**, 166102 (2011).
- (6) S. Gekle, and R. R. Netz, *J. Chem. Phys.* **137**, 104704 (2012).
- (7) S. Varghese, S. K. Kannam, J. S. Hansen, and S. P. Sathian, *Langmuir* **35**, 8159 (2019).

- (8) M. H. Motevaselian, and N. R. Aluru, *Acs Nano* **14**, 12761 (2020).
- (9) M. Rezaei, B. G. Mitterwallner, P. Loche, Y. Uematsu, R. R. Netz, and D. J. Bonthuis, *J. Phys. Chem. B* **125**, 4767 (2021).
- (10) D. V. Matyushov, J. Phys. Chem. B 125, 8282 (2021).
- (11) S. J. Cox, and P. L. Geissler, *Chem. Sci.* **13**, 9102 (2022).
- G. Gonella, E. H. G. Backus, Y. Nagata, D. J. Bonthuis, P. Loche, A. Schlaich, R. R.
- Netz, A. Kuhnle, I. T. McCrum, M. T. M. Koper, M. Wolf, B. Winter, G. Meijer, R. K. Campen, and M. Bonn, *Nature Rev. Chem.* **5**, 466 (2021).
- (13) J. F. Olivieri, J. T. Hynes, and D. Laage, J. Phys. Chem. Lett. 12, 4319 (2021).
- (14) N. Mulpuri, and D. Bratko, *J. Chem. Phys.* **158**, 134716 (2023).
- (15) D. Borgis, D. Laage, L. Belloni, and G. Jeanmairet, *Chem. Sci.* **14**, 11141 (2023).
- (16) M. T. Ajide, D. O'Carroll, and N. J. English, *Mol. Phys.* **121**, 2211404 (2023).
- (17) F. Moucka, D. Bratko, and A. Luzar, *J. Phys. Chem. C* **119**, 20416 (2015).
- (18) H. A. Stern, and S. E. Feller, *J. Chem. Phys.* **118**, 3401 (2003).
- (19) A. Schlaich, E. W. Knapp, and R. R. Netz, *Phys. Rev. Lett.* **117**, 048001 (2016).
- (20) D. Muñoz-Santiburcio, and D. Marx, *Chem. Rev.* **121**, 6293 (2021).
- (21) M. C. Andrade, and T. A. Pham, J. Phys. Chem. Lett. 14, 5560 (2023).
- (22) I. C. Yeh, and M. L. Berkowitz, *J. Chem. Phys.* **110**, 7935 (1999).
- (23) D. J. Bonthuis, S. Gekle, and R. R. Netz, *Langmuir* **28**, 7679 (2012).
- (24) K. Leung, *Nano Lett.* **23**, 8868 (2023).
- (25) C. Schaaf, and S. Gekle, *J. Chem. Phys.* **145**, 084091 (2016).
- S. Ruiz-Barragan, D. Munoz-Santiburcio, S. Korning, and D. Marx, *Phys. Chem. Chem. Phys.* **22**, 10833 (2020).
- S. Ruiz-Barragan, F. Sebastiani, P. Schienbein, J. Abraham, G. Schwaab, R. R. Nair, M. Havenith, and D. Marx, *Phys. Chem. Chem. Phys.* **24**, 24734 (2022).
- P. G. Kusalik, M. E. Gracheva, S. Shaik, and N. J. English, *Physical Chemistry Chemical Physics* **24**, 28660 (2022).
- <sup>(29)</sup> S. M. Sarhangi, M. M. Waskasi, S. M. Hashemianzadeh, and D. V. Matyushov, *J. Phys. Chem. B* **123**, 3135 (2019).
- (30) D. V. Matyushov, J. Phys. Chem. B **128**, 2930 (2024).
- (31) M. von Domaros, D. Bratko, B. Kirchner, and A. Luzar, *J. Phys. Chem. B* **117**, 4561 (2013).
- (32) Y. W. Zhang, H. B. de Aguiar, J. T. Hynes, and D. Laage, *J. Phys. Chem. Lett.* **11**, 624 (2020).
- (33) C. R. Song, and P. S. Wang, *Rev. Sci. Instrum.* **81**, 054702 (2010).
- (34) L. Y. Qing, S. L. Zhao, and Z. G. Wang, J. Phys. Chem. B 125, 625 (2021).
- (35) H. J. Butt, *Biophysical Journal* **63**, 578 (1992).
- (36) T. Fuhs, L. H. Klausen, S. M. Sonderskov, X. J. Han, and M. D. Dong, *Nanoscale* **10**, 4538 (2018).
- (37) D. Bratko, C. E. Woodward, and A. Luzar, *J. Chem. Phys.* **95**, 5318 (1991).
- (38) D. Bratko, and D. Dolar, J. Chem. Phys. **80**, 5782 (1984).
- (39) D. Bratko, and V. Vlachy, *Chem. Phys. Lett.* **115**, 294 (1985).
- (40) B. S. Jabes, D. Bratko, and A. Luzar, *J. Chem. Phys.* **148** (2018).
- (41) V. Ballenegger, and J. P. Hansen, *J. Chem. Phys.* **122**, 114711 (2005).
- (42) I. C. Yeh, and M. L. Berkowitz, *J. Chem. Phys.* **111**, 3155 (1999).

- N. Ojaghlou, D. Bratko, M. Salanne, M. Shafiei, and A. Luzar, *ACS Nano* **14**, 7987 (2020).
- <sup>(44)</sup> D. Bratko, R. A. Curtis, H. W. Blanch, and J. M. Prausnitz, *J. Chem. Phys.* **115**, 3873 (2001).
- <sup>(45)</sup> F. Moucka, D. Bratko, and A. Luzar, *J. Chem. Phys.* **142**, 124705 (2015).
- (46) D. Bratko, *Molecules* **29** (2024).
- (47) D. Vanzo, D. Bratko, and A. Luzar, J. Chem. Phys. **140**, 074710 (2014).
- (48) C. Calero, and G. Franzese, *J. Mol. Lig.* **317**, 114027 (2020).
- (49) J. Driskill, D. Vanzo, D. Bratko, and A. Luzar, J. Chem. Phys. **141**, 18C517 (2014).
- (50) S. Ruiz-Barragan, H. Forbert, and D. Marx, *Phys. Chem. Chem. Phys.* **25**, 28119 (2023).
- (51) H. J. C. Berendsen, J. R. Grigera, and T. P. Straatsma, *J. Phys. Chem.* **91**, 6269 (1987).
- (52) C. Vega, and J. L. F. Abascal, *Phys. Chem. Chem. Phys.* **13**, 19663 (2011).
- W. L. Jorgensen, D. S. Maxwell, and J. TiradoRives, *Journal of the American Chemical Society* **118**, 11225 (1996).
- <sup>(54)</sup> W. L. Jorgensen, M. M. Ghahremanpour, A. Saar, and J. Tirado-Rives, *J. Phys. Chem. B* **128**, 250 (2023).
- <sup>(55)</sup> R. L. Jaffe, P. Gonnet, T. Werder, J. H. Walther, and P. Koumoutsakos, *Mol. Simul.* **30**, 205 (2004).
- (56) R. P. Misra, and D. Blankschtein, J. Phys. Chem. C 121, 28166 (2017).
- <sup>(57)</sup> D. Bratko, C. D. Daub, K. Leung, and A. Luzar, *J. Am. Chem. Soc.* **129**, 2504 (2007).
- <sup>(58)</sup> J. R. Choudhuri, D. Vanzo, P. A. Madden, M. Salanne, D. Bratko, and A. Luzar, *Acs Nano* **10**, 8536 (2016).
- (59) D. Vanzo, D. Bratko, and A. Luzar, *J. Chem. Phys.* **137**, 034707 (2012).
- D. Van der Spoel, E. Lindahl, B. Hess, G. Groenhof, A. E. Mark, and H. J. C. Berendsen, *J. Comput. Chem.* **26**, 1701 (2005).
- (61) T. Darden, D. York, and L. Pedersen, *J. Chem. Phys.* **98**, 10089 (1993).
- (62) G. Bussi, D. Donadio, and M. Parrinello, *J. Chem. Phys.* **126** (2007).
- (63) B. Hess, H. Bekker, H. J. C. Berendsen, and J. Fraaije, *J. Comput. Chem.* **18**, 1463 (1997).
- (64) B. Hess, J. Chem. Theory Comput. 4, 116 (2008).
- (65) S. De Luca, S. K. Kannam, B. D. Todd, F. Frascoli, J. S. Hansen, and P. J. Daivis, *Langmuir* **32**, 4765 (2016).
- (66) C. Zhang, J. Chem. Phys. **148** 156101 (2018).
- (67) P. Loche, C. Ayaz, A. Wolde-Kidan, A. Schlaich, and R. R. Netz, *J. Phys. Chem. B* **124**, 4365 (2020).
- (68) I. Popov, P. Ben Ishai, A. Khamzin, and Y. Feldman, *Phys. Chem. Chem. Phys.* **18**, 13941 (2016).
- (69) D. Bratko, A. K. Chakraborty, and E. I. Shakhnovich, *Phys. Rev. Lett.* **76**, 1844 (1996).
- (70) I. M. Svishchev, and P. G. Kusalik, *J. Am. Chem. Soc.* **118**, 649 (1996).
- (71) R. Zangi, and A. E. Mark, *J. Chem. Phys.* **120**, 7123 (2004).
- (72) J. Y. Yan, and G. N. Patey, *J. Phys. Chem. Lett.* **2**, 2555 (2011).
- (73) J. Y. Yan, S. D. Overduin, and G. N. Patey, J. Chem. Phys. **141**, 074501 (2014).
- P. J. Turner, Xmgrace 5.1.19, Oregon Grad. Inst. Sci. Technol., Beaverton 2, 19 (2005).
- (75) S. Mondal, and B. Bagchi, *J. Chem. Phys.* **154** (2021).
- <sup>(76)</sup> Y. W. Zhang, G. Stirnemann, J. T. Hynes, and D. Laage, *Phys. Chem. Chem. Phys.* **22**, 10581 (2020).

- (77) J. F. Olivieri, J. T. Hynes, and D. Laage, *Faraday Discuss.* **249**, 289 (2024).
- (78) D. Bratko, A. Striolo, J. Z. Wu, H. W. Blanch, and J. M. Prausnitz, *J. Phys. Chem. B* **106**, 2714 (2002).
- (79) M. R. L. Becker, P.; Bonthuis, D. J.; Mouhanna, D.; Netz, R. R.; Berthoumieux, H., *Soft. Cond. Matt.*, https://doi.org/10.48550/arXiv.2303.14846 (2023).
- (80) G. D. Phillies, J. Chem. Phys. **60**, 2721 (1974).